

Full length article



Thermo-responsive and shape-morphing CF/GF composite skin: Full-field experimental measurement, theoretical prediction, and finite element analysis

Jamal Seyyed Monfared Zanjani^{a,*}, Pouya Yousefi Louyeh^{b,c,d}, Isa Emami Tabrizi^{b,c,d},
Abdulrahman Saeed Al-Nadhari^b, Mehmet Yildiz^{b,c,d,**}

^a Faculty of Engineering Technology, University of Twente, 7500AE Enschede, the Netherlands

^b Faculty of Engineering and Natural Sciences, Sabanci University, Tuzla, 34596, Istanbul, Turkey

^c Integrated Manufacturing Technologies Research and Application Center, Sabanci University, Tuzla, Istanbul, 34956, Turkey

^d Composite Technologies Center of Excellence, Sabanci University-Kordsa, Istanbul Technology Development Zone, Sanayi Mah. Teknopark Blvd. No: 1/1B, Pendik, 34906, Istanbul, Turkey

ARTICLE INFO

Keywords:

Shape morphing composites
Residual thermal stress
Digital Image Correlation
Adaptive composite skin
Finite element analysis (FEA)

ABSTRACT

Shape morphing is an attractive functionality for fibre reinforced composites. Shape morphing composites can adopt various shapes and undergo different shape morphologies in response to a set of external stimuli. One of the approaches to attain shape morphing materials is through fabrication of multi-layered and asymmetric composites where morphing stems from structural anisotropy. In this work, asymmetric hybrid carbon fibre/glass fibre/epoxy composites are manufactured in which a mismatch in the coefficient of thermal expansion between carbon and glass fibre layers and different fibre directions at each layer resulted in a thermo-responsive morphing behaviour. The full-field displacement of laminate surfaces at the temperature range of -30°C to 60°C are monitored using digital image correlation technique. Classical laminate theory and Timoshenko bimetallic strip formula are coupled with experimental observations to predict the radius of curvature for laminates at different temperatures. Furthermore, finite element analyses are performed to uncover the stress state in the laminates and identify the contributing mechanisms. This study contributes to the state of the art by elaborating on the relations between morphing performance with stiffness and thermal expansion of anisotropic fibre reinforced laminates and their connections to the microstructure.

1. Introduction

Fibre reinforced polymeric composites (FRPC) with “tailored” reinforcement, superior mechanical and physical properties, and lightweight are shown to be remarkable alternatives to heavy metallic and ceramic counterparts in critical applications [1–4]. The next technological wave in this area is to impart multi-functionalities into the composite parts. By doing so, polymeric composites not only provide lightweight materials for load-bearing structures but also perform additional functions [5]. Some of the currently available functionalities for FRPCs are electrical and thermal conductivity [6,7], de-icing [8], self-healing [9], and structural health monitoring [10]. Shape morphing is another attractive functionality of FRPCs in which a composite can

adopt various shapes and undergo different shape morphologies in response to a set of external stimuli if necessary [11,12].

Materials in nature with elegant and complex architectures and distinctive qualities have been a source of inspiration for many cutting edge novel functional materials [13]. The inspiration for morphing wings originated from Volant animals such as birds where their flexible wings give them the ability to control flight posture, minimize energy consumption and control aerodynamic performance in the air [14]. There are numerous other examples of natural materials that can autonomously change their shape in response to external stimuli such as pine cones and wheat awn in which anisotropic expansion characteristic in their cell walls due to the existence of oriented stiff cellulose fibrils leads to a shape change [15–17]. In these materials, the difference in

* Corresponding author.

** Corresponding author. Faculty of Engineering and Natural Sciences, Sabanci University, Tuzla, 34596, Istanbul, Turkey.

E-mail addresses: J.seyyedmonfaredzanjani@utwente.nl (J. Seyyed Monfared Zanjani), meyildiz@sabanciuniv.edu (M. Yildiz).

<https://doi.org/10.1016/j.tws.2020.106874>

Received 27 November 2019; Received in revised form 27 May 2020; Accepted 27 May 2020

Available online 31 December 2020

0263-8231/© 2020 The Authors.

Published by Elsevier Ltd.

This is an open access article under the CC BY-NC-ND license

(<http://creativecommons.org/licenses/by-nc-nd/4.0/>).

directional expansion of layers under an external stimulus due to the intrinsic anisotropy of materials induces a residual stress field over the structure thickness leading to out-of-plane deformations and a shape morphing behaviour [18]. Recently, there were several attempts to mimic such behaviours and impart morphing capabilities into the new generation of vehicles and aerodynamic structures [19].

Taking the idea from nature, shape morphing fibre reinforced composites have emerged based on the creation of composites with anisotropic microstructures [20]. Various theoretical and experimental studies were carried out in order to understand and predict the shape morphing in asymmetric composite structures [11,21–24]. One of the well-known approaches to attain shape morphing composites (SMC) is through the fabrication of multi-layered and asymmetric composites in which each layer is reinforced by unidirectional fibres while fibres direction is variable in each layer. In such laminates, thermal contraction upon cooling from elevated curing temperatures builds-up a locked-in residual stresses and forms out-of-plane deformation or so-called thermal buckling [25–27]. The thermal buckling in these materials is the basis for creating SMCs with shape adaptation capability under various temperature conditions or transition between multiple stable forms under a relatively small bending moment [28]. In addition, morphing structures are currently used in applications such as adaptive helicopter rotor blades [29,30], continuous morphing wing [31], and automotive fender skirts and many more [32]. However, having fibre directionality as the only driving force for morphing limits the possible shape configurations and the level of morphing for advanced applications [33]. Furthermore, the morphing effect on hybrid composites with different fibre materials and directions are currently unknown and due to geometric complexities of SMCs, and models validated through experiments are needed to predict their behaviour.

In this study, CF/GF composites with different fibre directions of $[90_G/0_C]$, $[30_G/-30_C]$, $[45_G/-45_C]$, and $[60_G/-60_C]$ were manufactured and their morphing capabilities were monitored by Digital Image Correlation (DIC) technique at temperature ranging from -30 to 60 °C. Classical laminate theory (CLT) and Timoshenko bimetallic strip formula were adapted and coupled to explain the DIC observations and to predict the laminates behaviour under various conditions. Moreover, finite element analysis (FEA) is performed to simulate thermal buckling and morphing in composite laminates and verify the experimental measurements of morphing behaviour of initially curved plates. The coupling of DIC measurements, with theoretical prediction and FEA, provided deeper insight into mechanisms involved in morphing behaviour of fibre reinforced composites and enabled a correlation between their microstructure and macro-behaviour.

2. Experimental and methods

2.1. Materials and composite preparation

Unidirectional (UD) carbon fibre (CF)/epoxy and glass fibre (GF)/epoxy prepregs were supplied by Kordsa Company used for the composite manufacturing. The CF/epoxy prepreg contains a unidirectional (UD) fabric with a dry areal weight of 300 ± 10 gsm produced by DowAksa-A49 12K fibres and epoxy resin content of 37 ± 2 wt%. The GF/epoxy prepreg includes fabric with a dry areal weight of 330 gsm (283 gsm, 1200 tex glass in 0° ; 37 gsm, 68 tex glass in 90° direction; and 10 gsm 76 dtex polyester stitches) from Metyx Composites and with 37 ± 3 wt% epoxy resin. The matrix material in both prepreg types is hot-melt resin composed of structural epoxy resin, dicyandiamide hardener, and urone-based accelerator. This matrix is a toughened, 130 °C cure epoxy resin with Young's modulus of 2.6 GPa, the tensile

strength of 36 MPa, shear modulus of 974 MPa, elongation at break of 2% and $T_g \geq 130$ °C (data provided by the manufacturer). The morphing composites were produced through vacuum bagging method on a stainless steel mould surface pre-treated by sealer and release agents. The prepared laminates manufactured by using a layer of UD GF/epoxy and a layer of CF/epoxy prepregs with dimensions of 170 mm in width \times 250 mm in length, where fibres alignments were $[90_G/0_C]$, $[30_G/-30_C]$, $[45_G/-45_C]$, and $[60_G/-60_C]$ as schematically are shown in Fig. 1a–d. In all laminates, GF/epoxy prepreg was laid on the mould surface and CF prepreg was placed on top of it. The vacuum bagging assembly was completed by a nylon peel ply, breather fabric (150 gsm) and enclosed by a METYX-VBF100BT65MIC vacuum bag sealed along the mould edges and connected to an air suction pump through a vacuum valve as shown schematically in Fig. 1e. Prior to curing, the laminates were de-bulked under vacuum for 30 min to remove entrapped air from lay-up and to consolidate the laminates. Next, the mould was heated up to 130 °C and kept for 3 h to achieve fully cured specimens considering the manufacturer recommendations. Afterward, the system was slowly cooled down to the room temperature while still under vacuum. Furthermore, sole CF and GF laminates were manufactured using eight layers of each prepreg using the same procedure to determine the coefficient of thermal expansion (CTE) and mechanical properties of individual prepreg types.

2.2. Material characterization

The mechanical properties namely tensile modulus, Poisson's ratio, and shear modulus for each of CF and GF composites were determined using Instron 5982- 100 kN Electromechanical Test System (UTM) with 100 kN load cells. The tensile tests were conducted at a constant cross-head speed of 2 mm/min in accordance with ASTM D5083-02 standard. The strain measurements during the tensile test were performed by using KYOWA KFG350 Ω Biaxial, $0^\circ/90^\circ$ foil strain gages. Shear modulus was measured applying the Iosipescu shear test (v-notched shear test) in compliance to ASTM D5379 standard. The density of GF and CF composite laminates were measured by using Buoyancy (Archimedes) method in conformity with ASTM D2734. Nikon-LV100ND optical microscope was used to study the cross-section of specimens, hence determining the volume fraction of fibres and thickness of layers. The average fibre volume fraction was obtained as 56.75% and 57.25% for the CF and GF laminas while the average thickness was 270 μ m and 200 μ m, respectively (see Table S1 for more details). The CTE of GF and CF composites in longitudinal and transverse directions were measured inside a Vötsch- VC³-7150 conditioning chamber using strain gauges and following the procedure given in Ref. [21] and further described in Refs. [11,34] by using KYOWA KFG350 Ω uniaxial strain gauges were attached to the surface of each specimen and using an aluminium sample with CTE of $24 \times 10^{-6}/^\circ\text{C}$ as the reference. Both strain gauges and thermocouples were interrogated with National Instrument data logger system with a LabVIEW interface. Fig. 2 exhibits the CTE of GF and CF laminates at two directions of parallel and perpendicular to fibre direction and its temperature dependency. Table 1 summarizes the characteristic properties of GF and CF composites which are implemented in the theoretical predictions and finite element analysis (FEA).

2.3. Full-field displacement measurement by digital image correlation (DIC)

DIC is used as a full-field measurement technique to obtain the displacement values at each point of the laminates surface due to thermal buckling. Measurement in DIC system assumes that any changes in

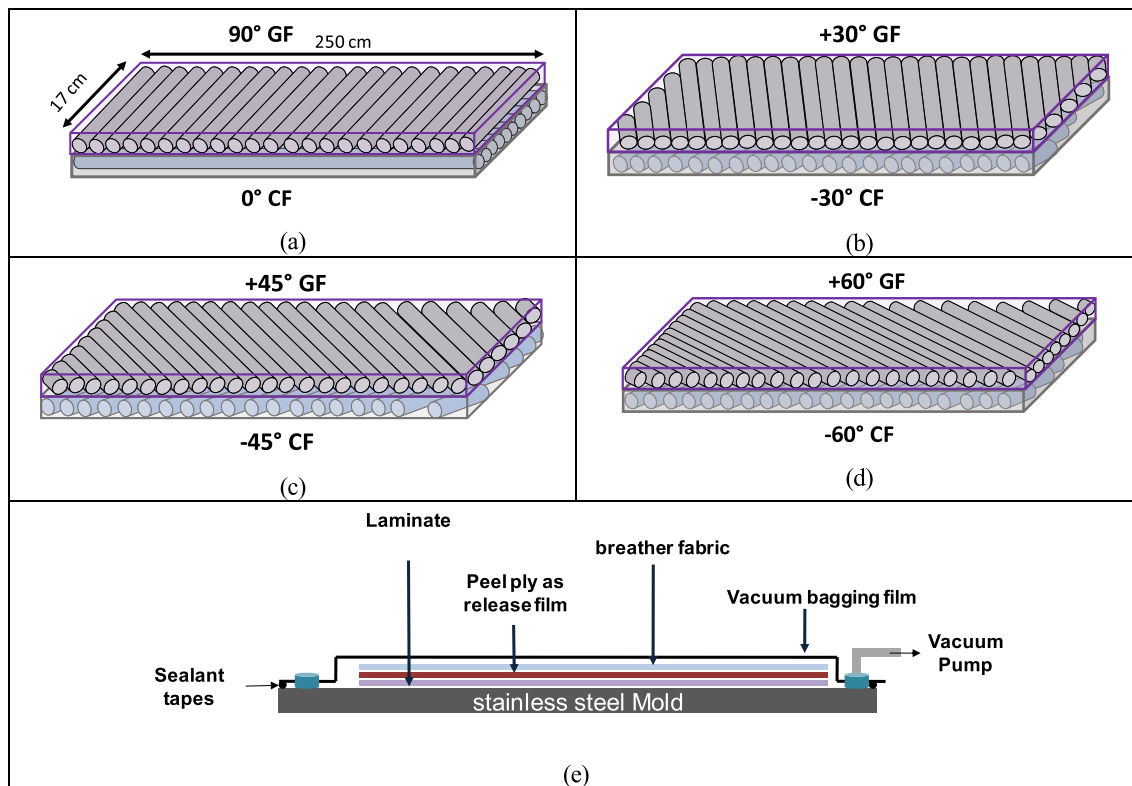


Fig. 1. A schematic representation of stacking sequence of GF and CF layers in the laminates namely (a) [90_G/0_C], (b) [30_G/-30_C], (c) [45_G,-45_C], and (d) [60_G/-60_C] and (e) composite manufacturing assembly of vacuum bagging of prepregs.

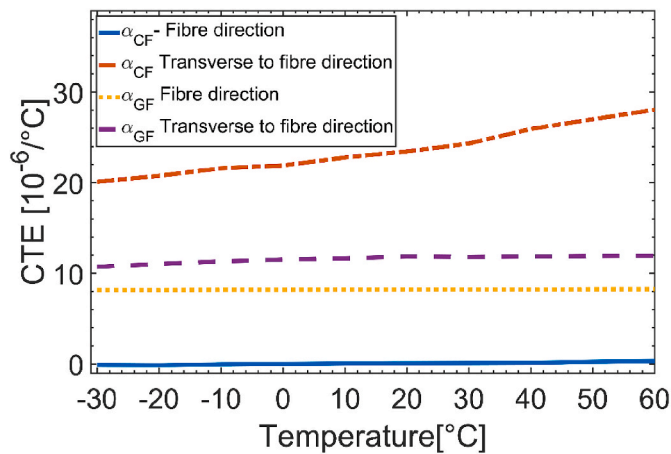


Fig. 2. CTE vs. temperature curves for CF and GF along and transverse to fibre direction.

material shape occurs through translational or rotational displacements which are reflected into the correlated images taken by DIC sensors (cameras). To have an enough range of colour shades and to ensure adequate contrast on the surface of the specimen, speckle pattern

consisting of randomly painted white and black points are created on the surface of the material before deformation. Then the DIC software divides the image before deformation into small subsets with a specified pixel size called “Facet points”. During deformation each predefined subset is followed (distinguished) by cameras within a specified neighbouring distance in pixels, i.e. “Step size” or “Point distance”. The size of defined Facet points and step sizes can directly change the computational time and accuracy of calculations for each point on the surface [35]. As seen in Fig. 3a for a Facet point with a size of 25 × 25-pixels, the software tracks the stretch and rotation of every single Facet and uses a computational algorithm to obtain the displacement at each point using a local tangent coordinate system.

In this investigation, DIC system manufactured by GOM GmbH is used which is equipped with couple of 12 Megapixel sensors with 100 mm lenses and employs ARAMIS professional software for computational processes of displacement fields. Since thermal buckling of the hybrid composite laminates consists of out of plane displacements, DIC system was calibrated in 3D mode, i.e. using two cameras in a stereo configuration with a depth of field above 400 mm. The calibration procedure was performed using standard coded calibration object designated as CP20 350 × 280 by the manufacturer in which a maximum area of 300 mm × 400 mm can be monitored. The distance between two sensors was set to 1376 mm and the working distance between the sensors and calibration object was set to 1890 mm as per the recommendation of the DIC manufacturer. The calibration was

Table 1
Summary of the physical and mechanical properties of solo GF and CF laminates.

	Density ρ [g/cm ³]	Elastic modulus fibre direction E_1 [GPa]	Elastic modulus transverse to fibre direction E_2 [GPa]	Poisson's Ratio ν_{12}	Shear Modulus G_{12} [GPa]
GF Laminate	1.744	34.15	12.33	0.23	3.80
CF Laminate	1.541	133.20	7.77	0.3	2.29

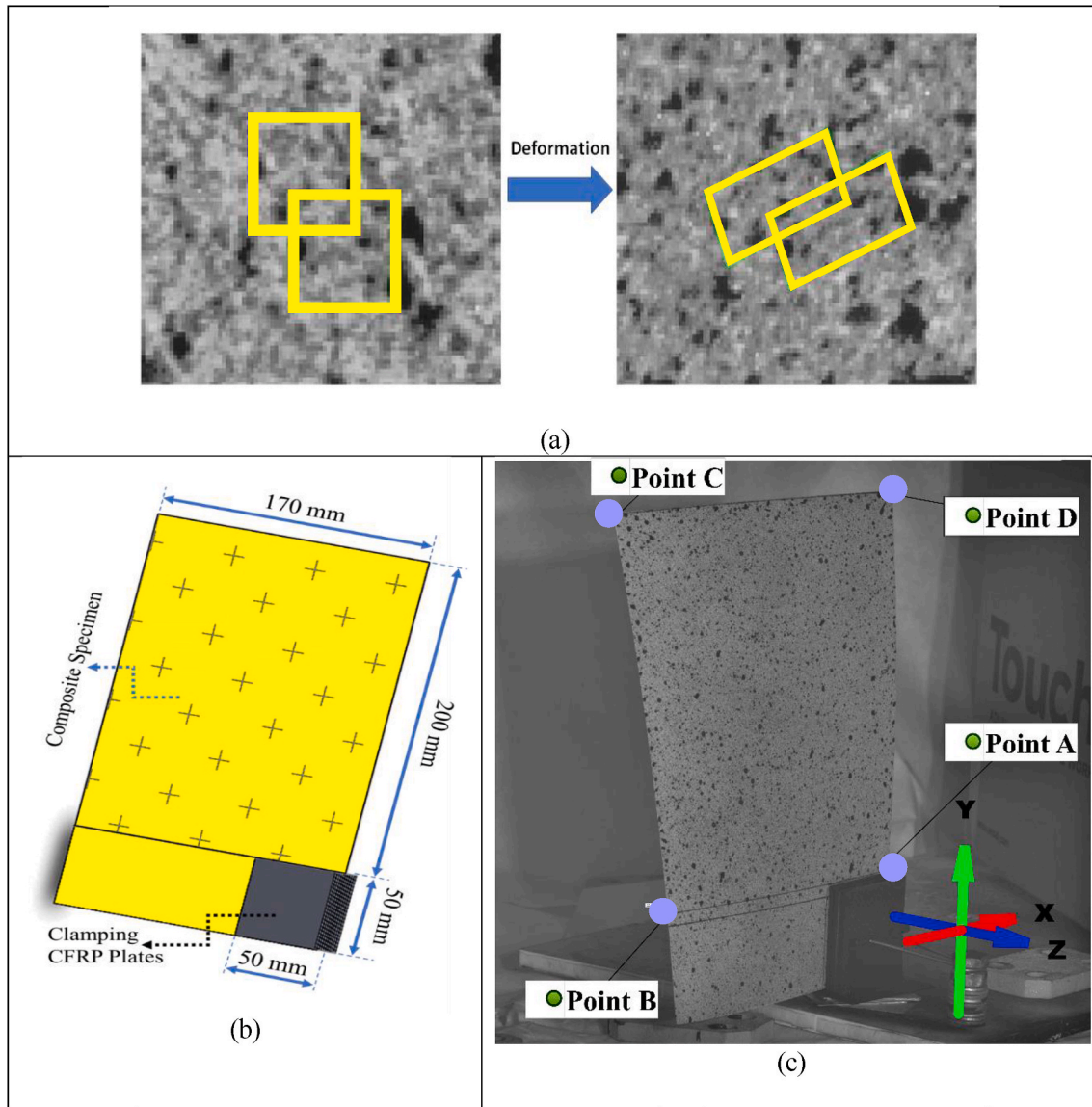


Fig. 3. (a) Facet stretch and rotation during a deformation, (b) Typical morphing laminate geometry, fixture and dimensions, (c) Morphing laminate with speckle pattern in DIC test condition.

conducted in single snap mode, and results showed calibration deviation of 0.025 mm and scale deviation of 0.004 pixels which are below the criteria demanded by software as 0.05 mm and 0.05 pixel, respectively. During the calibration procedure the depth of field for sensors is set to be ≥ 400 mm, thus measurement of thermal buckling is assured for high out of plane displacements.

To conduct the experiments, speckle pattern was applied on the surface, i.e. GF layer, of the samples with the size 50 mm \times 170 mm, using white and black paint sprays. The prepared laminates are clamped from the lower right corner using 50 mm \times 50 mm carbon fibre reinforced polymer (CFRP) plates as seen in Fig. 3b and c. Using CFRP plates as a tangent clamping material prevented the direct contact of metallic clamps with laminates, hence eliminated the possible effect of high coefficient of thermal expansion imposed by metallic parts. Moreover, small CFRP plates ensured that a certain region of the laminates would never deform during temperature variation thus, creating a reliable constraint to be defined for further numerical simulations. The clamped laminates were fastened on a polymeric substrate and the assembled set up was put inside Vötsch- VC³-7150 conditioning chamber. The DIC system was positioned in front of the door of the chamber and distance

between the sample and full field measurement sensors were set to 1890 mm since it was set as working distance during the calibration procedure.

All necessary preventive measures were made to control ambient light noise and obtain high contrast images. An initial reference image in undeformed state of laminate was taken from the area of interest with the size of 200 mm \times 170 mm indicated by plus signs as it is shown in Fig. 3b. The corners of the area of interest were named by letters of A to D (see Fig. 3c) to facilitate further discussions in the result section. Facet points of 25 \times 25 pixels and step size of 19 \times 19 pixels were used to define the surface in DIC system [35]. The temperature ramp of 2 °C/min was used to change the temperature inside the chamber, the system was kept at the set temperature for 15 min to ensure homogenization of temperature all over the laminate and its consistency within the chamber. DIC images were taken at every 10 °C between -30 °C and 60 °C.

2.4. Classical laminate theory and numerical simulation by ABAQUS

The total strains induced on each lamina (due to thermal expansion

and gravity) according to the Classical Lamination Plate Theory (CLPT) for a 2D object can be written in a compact vector-matrix form as [36]:

$$\begin{Bmatrix} \varepsilon_1 \\ \varepsilon_2 \\ \frac{1}{2}\varepsilon_6 \end{Bmatrix} = \begin{bmatrix} S_{11} & S_{12} & 0 \\ S_{12} & S_{22} & 0 \\ 0 & 0 & S_{66} \end{bmatrix} \begin{Bmatrix} \sigma_1 \\ \sigma_2 \\ \sigma_6 \end{Bmatrix} + \begin{Bmatrix} \alpha_1 \\ \alpha_2 \\ 0 \end{Bmatrix} \Delta T \quad (1)$$

where ε_i ($i = 1, 2, 6$) are the lamina strains, σ_i are the lamina stresses, α_i are the lamina thermal expansion coefficients, ΔT is the temperature change, and S_{ij} ($i, j = 1, 2, 6$) are the material compliance parameters. The laminate and lamina strains can be related to the transformation matrix $[T]^{-1}$ as following:

$$[T]^{-1} = \begin{bmatrix} c^2 & s^2 & -2cs \\ s^2 & c^2 & 2cs \\ cs & -cs & c^2 - s^2 \end{bmatrix} \quad (2)$$

Where $c = \cos(\theta)$, $s = \sin(\theta)$, and θ is the angle measured from the laminate to the material coordinate system. By using the transformation matrix, Eq (2), the strains can be rotated to the laminate coordinates as:

$$\begin{Bmatrix} \varepsilon_x \\ \varepsilon_y \\ \frac{1}{2}\varepsilon_{xy} \end{Bmatrix} = \begin{bmatrix} \bar{S}_{11} & \bar{S}_{12} & \bar{S}_{16} \\ \bar{S}_{12} & \bar{S}_{22} & \bar{S}_{26} \\ \bar{S}_{16} & \bar{S}_{26} & \bar{S}_{66} \end{bmatrix} \begin{Bmatrix} \sigma_x \\ \sigma_y \\ \sigma_{xy} \end{Bmatrix} + \begin{Bmatrix} \alpha_x \\ \alpha_y \\ \alpha_{xy} \end{Bmatrix} \Delta T \quad (3)$$

where ε_i ($i = x, y, xy$) are the laminate strains, σ_i are the laminate stresses, α_i are the laminate thermal expansion coefficients, and \bar{S}_{ij} ($i, j = 1, 2, 6$) are the laminate compliance coefficients. Since $\alpha \Delta T$ represents strains, the vector α transforms like strains in the following form:

$$\begin{Bmatrix} \alpha_x \\ \alpha_y \\ \frac{1}{2}\alpha_{xy} \end{Bmatrix} = [T]^{-1} \begin{Bmatrix} \alpha_1 \\ \alpha_2 \\ 0 \end{Bmatrix} \quad (4)$$

The laminate constitutive relations can be written as:

$$\begin{Bmatrix} N_x \\ N_y \\ N_{xy} \\ M_x \\ M_y \\ M_{xy} \end{Bmatrix} = \begin{bmatrix} A_{11} & A_{12} & A_{16} & B_{11} & B_{12} & B_{16} \\ A_{12} & A_{22} & A_{26} & B_{12} & B_{22} & B_{26} \\ A_{16} & A_{26} & A_{66} & B_{16} & B_{26} & B_{66} \\ B_{11} & B_{12} & B_{16} & D_{11} & D_{12} & D_{16} \\ B_{12} & B_{22} & B_{26} & D_{12} & D_{22} & D_{26} \\ B_{16} & B_{26} & B_{66} & D_{16} & D_{26} & D_{66} \end{bmatrix} \begin{Bmatrix} \varepsilon_x^o \\ \varepsilon_y^o \\ \gamma_{xy}^o \\ \kappa_x \\ \kappa_y \\ \kappa_{xy} \end{Bmatrix} - \begin{Bmatrix} N_x^T \\ N_y^T \\ N_{xy}^T \\ M_x^T \\ M_y^T \\ M_{xy}^T \end{Bmatrix} \quad (5)$$

where A_{ij} are the extensional stiffnesses, D_{ij} are the bending stiffnesses, and B_{ij} are the bending extensional coupling stiffness components, which are defined in terms of lamina stiffness according to the reference [36]. The thermal forces and moments per unit length in Eq (5) are defined as:

$$\{N^T\} = \sum_{k=1}^N \int_{z_k}^{z_{k+1}} [\bar{Q}]^{(k)} \{\bar{\alpha}\}^{(k)} \Delta T dz \quad (6)$$

$$\{M^T\} = \sum_{k=1}^N \int_{z_k}^{z_{k+1}} [\bar{Q}]^{(k)} \{\bar{\alpha}\}^{(k)} \Delta T z dz \quad (7)$$

where $[\bar{Q}]^{(k)}$ is the transformed reduced stiffness matrix of the k^{th} layer, and N is the total number of layers. The thermal loads are either added to the mechanical loads or moved to the left-hand-side of Eq (5) to find the curvatures and mid-surface strains. Therefore, the strain values at any location through the thickness of the laminate can be computed by:

$$\begin{Bmatrix} \varepsilon_x \\ \varepsilon_y \\ \gamma_{xy} \end{Bmatrix} = \begin{Bmatrix} \varepsilon_x^o \\ \varepsilon_y^o \\ \gamma_{xy}^o \end{Bmatrix} + z \begin{Bmatrix} \kappa_x \\ \kappa_y \\ \kappa_{xy} \end{Bmatrix} \quad (8)$$

These formulations are used to calculate the CTE and modulus of laminates at different angles and predict the curvature of each morphing laminate and their responses to temperature. In order to include the effect of residual stress in simulations, the curved shape laminates obtained from DIC measurements at 30 °C are used as an input for FEA simulations. Material properties including pure resin and prepregs utilized in the modelling are obtained from datasheet of the resin and our experiments as mentioned in detail in section 2.2. ABAQUS™ as a powerful commercial software which uses a non-linear finite element method to predict the behaviour was used to model the morphing behaviour of asymmetric GF/CF laminates with different fibre orientations and under various environmental conditions. Laminates were modelled using standard 8-noded doubly curved thin quadrilateral shell element, reduced integration, with 5° of freedom per node (S8R5) having quadratic geometric order with an approximate global size of 5 mm. Each model used nearly 1320 number of elements. Mesh refinement study was performed to ensure the accuracy of the results by considering the suitable computational time. Fig. S7 provided in the supplementary document shows the magnitude of deflection of the laminate $[G_{90}, C_0]$ with respect to various approximate global element size in two different temperatures of -30 and +60 °C, in which maximum deflections were detected. This illuminates the independency of simulation results to the mesh size. The mesh size on the rest of the laminates were kept the same as they have the same plate size. Similar to the experimental morphing measurement, each plate is clamped at the right bottom side with about 50 mm length. As shown in Fig. 3, each laminate is fixed by a rectangular grip at the bottom right corner. In order to simplify the model, only the region above the grip is considered for simulations. The lower part of the plate has a negligible effect on buckling results since the difference between CTEs causes the deformation and the fixture at the bottom significantly takes the freedom of that region from buckling. The temperature change process is simulated by using general static steps with considering the non-linear effects on large displacements and automatic stabilization. The full-newton technique is applied with a direct equation solver.

3. Results and discussion

3.1. Properties dependence to the fibre direction

Herein, the morphing behaviour based on the warpages of laminates was originated from the anisotropic properties of laminates with asymmetric material properties and fibre configurations. Therefore, an estimate of the property variation with the change in fibre direction is essential to gain a comprehensive understanding of the effective parameters on the morphing functionality and to uncover the rule of microstructure on macro-performance. Therefore, classical laminate theory and transformation matrices were used to determine the elastic modulus and CTE dependencies to the fibre direction, as the most effective parameters driving the shape morphing capability. The elastic modulus in the direction of interest in a UD laminate can be obtained as [37]:

$$E_\theta = Q_{11} \cos^4(\theta) + Q_{22} \sin^4(\theta) + 2(Q_{12} + 2Q_{66}) \sin^2(\theta) \cos^2(\theta) \quad (9)$$

where Q_{ij} are stiffness matrix elements and θ is the angle between fibre

direction and the direction of interest ($\theta = 0^\circ$ means along the fibre direction and 90° means perpendicular to the fibre direction). In addition, CTE dependency to fibre direction can be obtained by using flexibility transformation matrix as:

$$\alpha_\theta = \alpha_1 \cos^2(\theta) + \alpha_2 \sin^2(\theta) \quad (10)$$

where α_1 and α_2 are CTE of laminate in fibre direction and transverse to fibre direction. Fig. 4a and b demonstrate the modulus and CTE changes for CF and GF laminates where θ values vary between -90° and 90° . From Fig. 4, it can be seen that the elastic modulus and CTE of the laminates are strongly dependant on the fibre angles. When the angle is 0° (loading along fibre direction), the modulus of the composites reaches its highest value while CTE is at its lowest while at $\theta = 90^\circ$ they are at the lowest and highest level, respectively.

In the following sections, based on observed morphing behaviour of different laminates and to facilitate the discussions on morphing behaviour curvature along B-C line for $[90_G/0_C]$ and curvature along A-C for $[30_G/-30_C]$, $[45_G/-45_C]$, and $[60_G/-60_C]$ laminates were selected as a comparison tool for further analysis (points are indicated in Fig. 3). Therefore, it is essential to comprehend the elastic modulus and CTE for each layer along these directions to understand the relations between microstructure and macro-scale properties in various laminates. In this regard, Fig. 5 shows the schematic of a laminate in which fibres are aligned with φ angle with respect to the long edge of the laminate (fibres orientation angle in laminates) and θ_{AC} is effective transformation angle (θ in Eqs (9) and (10)) to be used for calculating the elastic modulus and CTE in A-C direction which can be calculated as:

$$\theta_{AC} = \text{Arctan}\left(\frac{l_{CD}}{l_{AD}}\right) - \varphi \quad (11)$$

where l_{CD} and l_{AD} are lengths of the laminate in indicated directions. Merging the laminate properties presented in section 2.2 and Eqs (9)–(11), Table 2 summarizes the effective transformation angle, elastic modulus and CTE for $[30_G/-30_C]$, $[45_G/-45_C]$, and $[60_G/-60_C]$ at room temperature. Herein, the hybrid CF/GF allows wider variation in coupled CTE and stiffness values for laminates with varying directions compared to asymmetric laminates with solo fibre type which opens new morphing capability compared to single fibre type laminates.

3.2. Full-field shape morphing monitoring by DIC

The full-field deformation of the laminates was monitored by DIC. The initial warpage of laminates surface at the reference temperature of 30°C was captured and used as the reference for determining the consequent shape changes and to model them under various temperatures for four different laminates of $[90_G/0_C]$, $[30_G/-30_C]$, $[45_G/-45_C]$, and $[60_G/-60_C]$. Fig. 6 displays the laminates prepared for DIC monitoring with applied speckle patterns on the GF side. These laminates

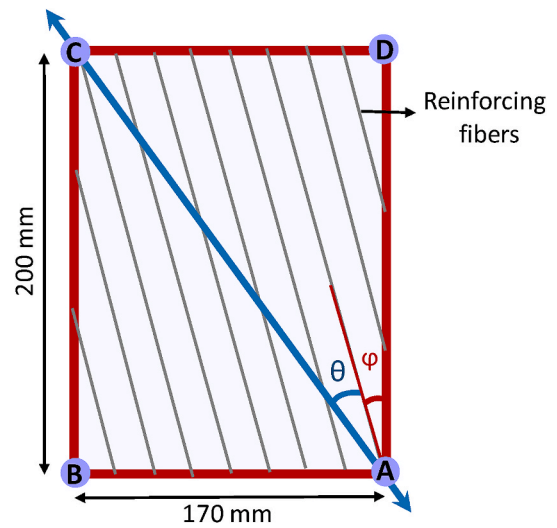


Fig. 5. Schematic presentation of fibre direction, φ angle with respect to the long edge of the laminate and θ is effective transformation angle.

Table 2
Effective angles, elastic modulus and CTE values in A-C diagonal direction.

Laminate	$[30_G/-30_C]$	$[45_G/-45_C]$	$[60_G/-60_C]$
$\theta_{AC} [^\circ]$ CF	70.36	85.36	100.36
$\theta_{AC} [^\circ]$ GF	10.36	-4.63	-19.6
E_{AC} [GPa] CF	9.02	7.77	7.80
E_{AC} [GPa] GF	32.55	33.88	28.68
α_{AC} [$10^{-6}/^\circ\text{C}$] CF	21.56	24.14	23.52
α_{AC} [$10^{-6}/^\circ\text{C}$] GF	8.34	8.25	8.63

were fixed from one edge to a rigid base plate and placed into the conditioning chamber with the temperature set to 30°C . The origin for the coordinate system is placed at the lower right corner of the area of interest where the specimen is fixed to the rigid bottom plate.

Fig. 7 shows the full-field deformation of laminates obtained by DIC which reveals the laminates morphing behaviour and their transition between temperatures of -30°C to 60°C (more details are available in Fig. S1). In Fig. 7 the trajectory of corner points (green spheres) exhibits the morphing path for each corner point while laminates state at extremum temperatures are presented. The point-A (points names are indicated in Fig. 3) did not show any displacement and consequently any movement path for the all laminates which reassures the assumption to consider it as a fixed point in the calculations and modelling. As seen in the scale bars of Fig. 7 the red colour represents high positive displacements out of the plane in “z” direction with respect to the reference

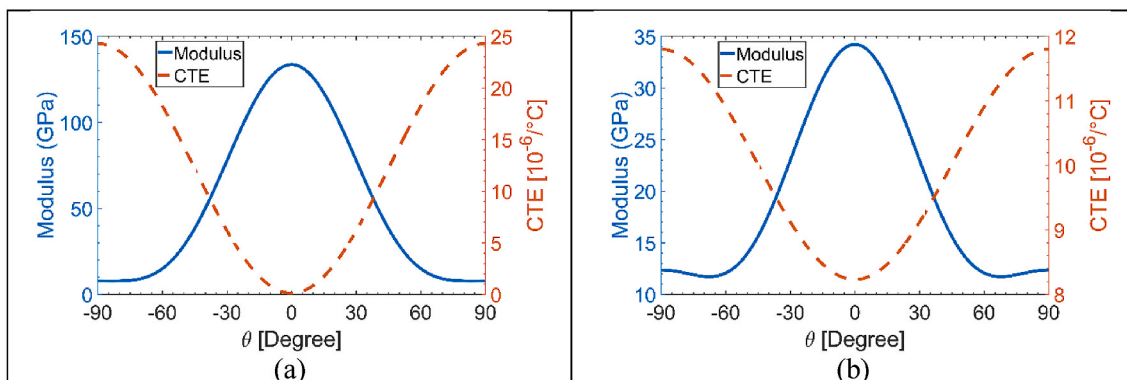


Fig. 4. Elastic modulus and CTE dependency to fibre directionality (θ) for (a) CF, and (b) GF laminates.

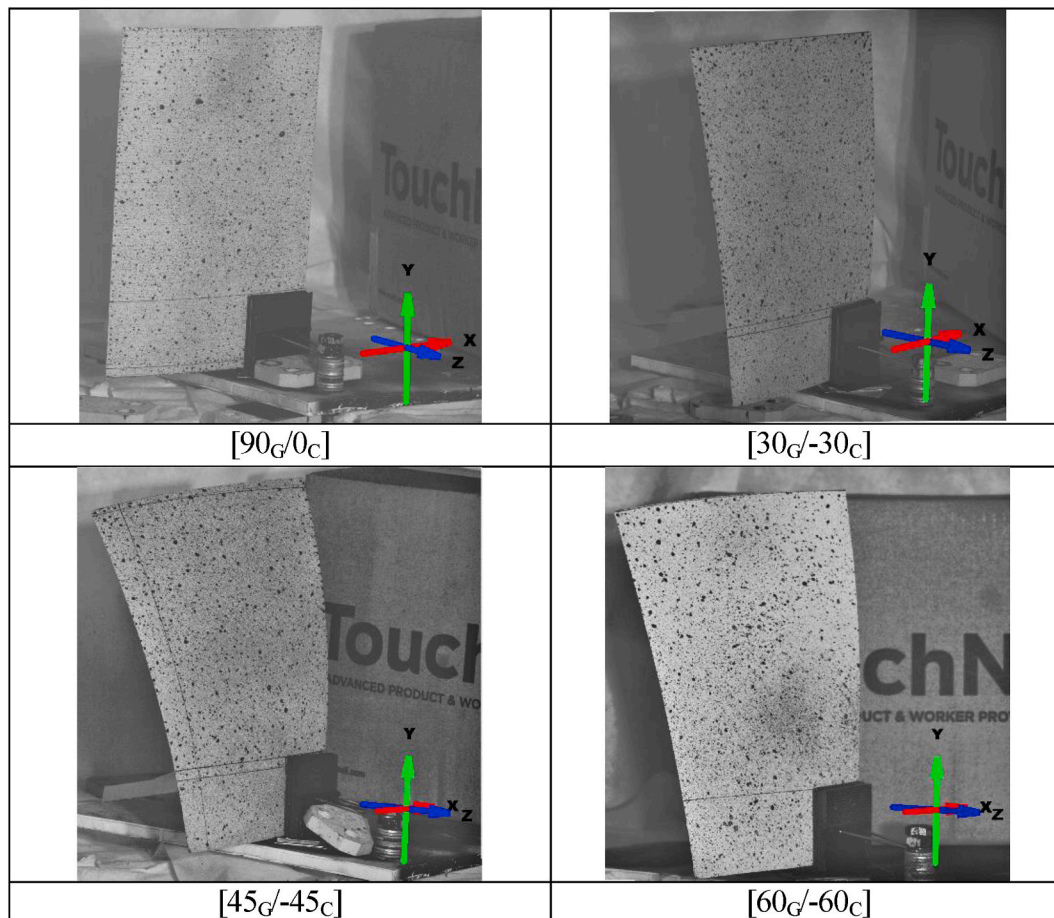


Fig. 6. Laminate prepared for DIC measurements inside the conditioning chamber with initial warpage at 30 °C.

position and blue colour demonstrates negative displacements.

In $[90_G/0_C]$ laminate, and through temperature manipulation, both point B and point C of the laminate were shifted in the X-Z plane which covered an arc of a circle with a radius of 88.27 mm and 78.05 mm and the swept arc length of 42.35 mm and 42.593 mm, respectively. Therefore, $[90_G/0_C]$ laminate morphing can be described as bending in the X-Y plane and around a parallel line to the A-D edge. This is expected behaviour in $[90_G/0_C]$ laminate as CF layer possess high CTE value of $20\text{--}28 \times 10^{-6}/^\circ\text{C}$ in lateral direction (perpendicular to fibre) which is in width of this laminate while CTE of GF lamina in width of this laminate (GF direction) is about $8 \times 10^{-6}/^\circ\text{C}$. Thus, higher contraction of CF lamina compared to the counterpart GF lamina in temperatures below 30 °C resulted in bending of the laminates at width creating lower radius of curvature of the arc connecting points C to D. On the other hand, at temperatures higher than 30 °C carbon layer expands and causes larger C-D arc radius. This can further be clarified by applying the classical beam-bending theory [38] by recognizing the glass layer in the tension side of laminates based on its curvature and which has been explained in our detailed study using FBG data elsewhere [11] where expansion of carbon layer reduced the tension forces and consequently increased the bending curvature of point C-D. Nevertheless, the contraction of CF layer by a reduction in the environment temperature exert higher tension and reduced the radius. The absence of any deformation in the length of $[90_G/0_C]$ laminate stemmed from the geometrical constraints applied by pre-deformed laminate which makes it stiff and resistant to the bending in length of the laminate.

In order to achieve laminates with higher morphing complexity, laminates with $[30_G/-30_C]$, $[45_G/-45_C]$, and $[60_G/-60_C]$ configurations were manufactured, and a set of unique morphing capabilities were obtained as shown in Fig. 7. The laminate with $[30_G/-30_C]$ fibre

orientations showed displacement paths in points B, C, and D in which points B and D had relatively low displacement compared to the point C which covers an arc of 103.36 mm associated with the displacement of -50 mm at -30 °C and 33 mm at 60 °C. Similarly, laminates of $[45_G/-45_C]$, and $[60_G/-60_C]$ showed relatively low displacements in point B and point D while having a large deformation in point C with displacements ranging from -50 mm to 52 mm and -40 mm to 25 mm between -30 °C and 60 °C, respectively. The morphing performances of each laminate are exhibited in Movies S1–S4 in the supplementary document. Table 3 summarizes the radius and arc length of displacement trajectories for all four types of laminates.

Supplementary video related to this article can be found at <https://doi.org/10.1016/j.tws.2020.106874>

3.3. Effect of fibre direction on morphing performance

As it is shown in Fig. 7 the overall morphing state of each laminate at any specific experiment temperature was monitored by DIC. However, to determine, quantify and analyse the fibres direction and temperature effect on the curvatures the surface data points obtained by DIC were used to define an osculating circle, as shown in Fig. 8a, from which the curvature of the laminate at each temperature and direction can be defined as $1/r$ where r is radius of the circle. The osculating circle was defined as a circle passing through diagonal of plates (A and C in Fig. 5) to get a unique and comparable radius of curvature in all configurations. It was observed that the dominant curvature in $[90_G/0_C]$ laminate was alongside A-B edge, therefore, the osculating circle for $[90_G/0_C]$ laminate was defined as the circle surface normal is parallel to A-D edge. For the rest of laminates, osculating circles were defined to paths through the A-C diagonal of laminates. Fig. 8b shows curvature for each laminate

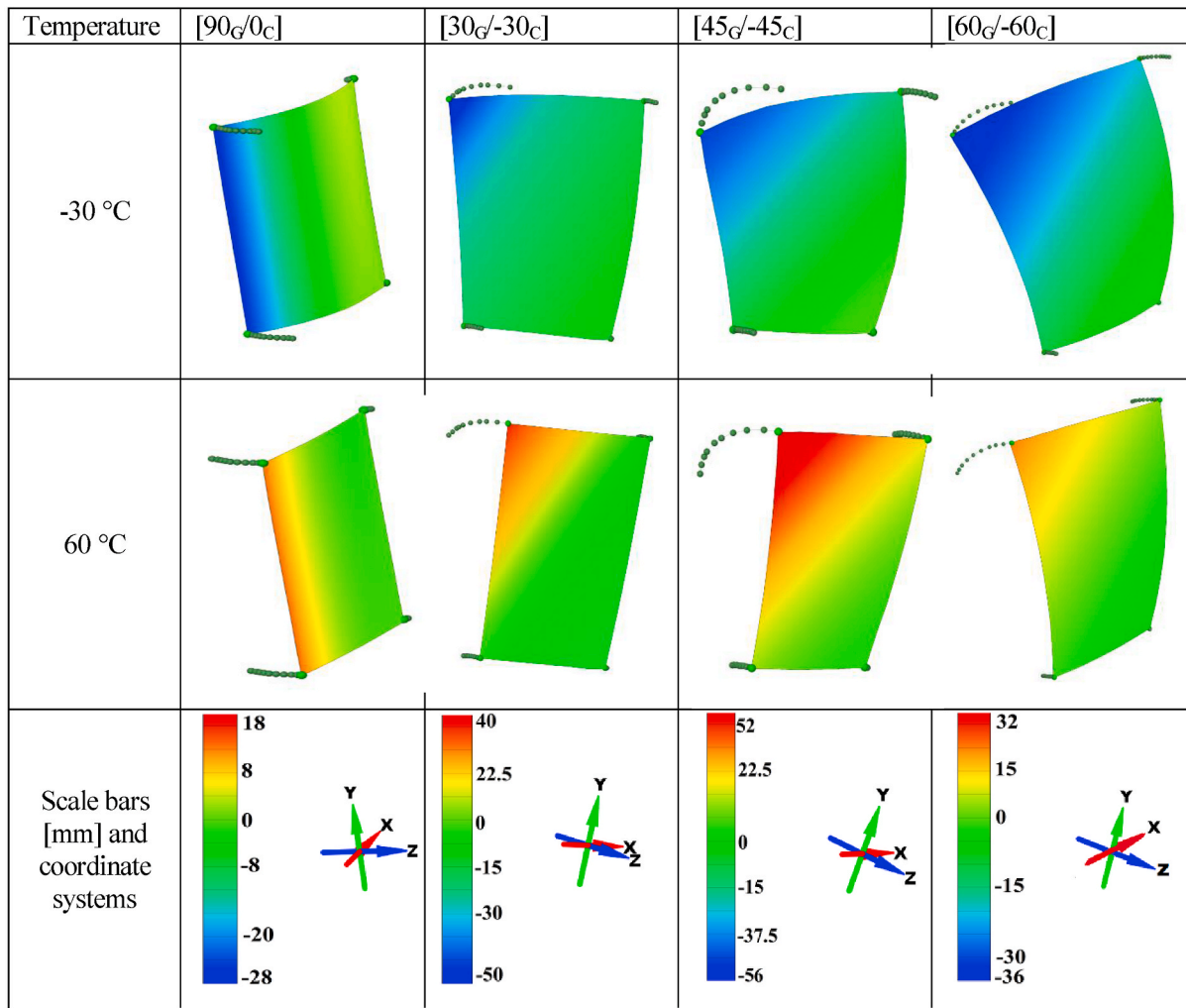


Fig. 7. Full-field morphing behaviour monitoring of laminates by DIC with different fibre directionally and their displacement paths between $-30\text{ }^{\circ}\text{C}$ and $60\text{ }^{\circ}\text{C}$.

Table 3
Radius and arc length of displacement trajectories.

	Radius [mm]			Arc Length [mm]		
	Point B	Point C	Point D	Point B	Point C	Point D
[90 _G /0 _C]	88.27	78.05	N/A	42.35	42.59	4.41
[30 _G /-30 _C]	52.35	151.54	27.83	23.10	103.36	16.42
[45 _G /-45 _C]	56.80	158.79	68.93	24.20	153.30	39.62
[60 _G /-60 _C]	39.95	168.68	106.80	11.40	99.66	32.85

at different experimental temperatures and its variations. It is worth noting that [90_G/0_C] laminate has the lowest curvature at each temperature in comparison to the other laminates, however, due to the difference in defining its osculating circle it is not comparable to the other laminates. For the rest of laminates, [30_G/-30_C] showed the minimum curvature value at all temperatures meaning that the radius of the osculating circle is higher than others. This is because of the higher modulus of CF layer and the lower difference in the CTE of in A-C diagonal of this laminates as it is presented in Table 2, thus lower bending forces and higher resistance for warpage is presented compared to [45_G/-45_C], and [60_G/-60_C] ones. In [45_G/-45_C], and [60_G/-60_C] laminates with relatively higher CTE difference and lower modulus in AC diagonal higher curvatures were obtained. However, due to changes in the difference of CTE (see Fig. 2) at temperatures below 10 °C, [45_G/-45_C] laminate possessed higher curvature and at temperatures above it [60_G/-60_C] laminate had the highest curvature. It was observed that

increasing the temperature brings about a decrease in curvature which is associated with the higher CTE in the transverse direction of CF layer at higher temperatures which resulted in greater expansion of CF layer when compared to GF layer (See Fig. 2 and Table 1). Note that, CF resides at the inner surface of the curved laminates because of its higher shrinkage during the cooling process and after curing at high temperature with respect to GF layer with lower CTE value displacement. Fig. 8b reveals a decreasing linear trend on the curvatures by an increase in temperature for all specimens which is correlated with the difference in CTE values of layers at AC direction and higher the difference more pronounced temperature dependency was observed. Table 4 summarizes the slope of lines fitted on curvature vs temperature data for each laminate.

3.4. Theoretical prediction of curvature

To theoretically calculate the radius of curvature of the composite, the classical Timoshenko formula initially developed for bimetallic strips subjected to thermal variation is adapted here [11,39–42], in the form of:

$$k = \frac{t \times \left[3 \times (1 + m)^2 + (1 + m + n) \times \left(m^2 + \frac{1}{(m \times n)} \right) \right]}{6 \times (\alpha_{2\theta} - \alpha_{1\theta}) \times (\Delta T) \times (1 + m)^2} \quad (12)$$

where k is the radius of curvature, $t = t_1 + t_2$ is total thickness of structure with t_1 and t_2 being the thickness of each layer, $m = t_1/t_2$, $n = E_{1\theta}/E_{2\theta}$

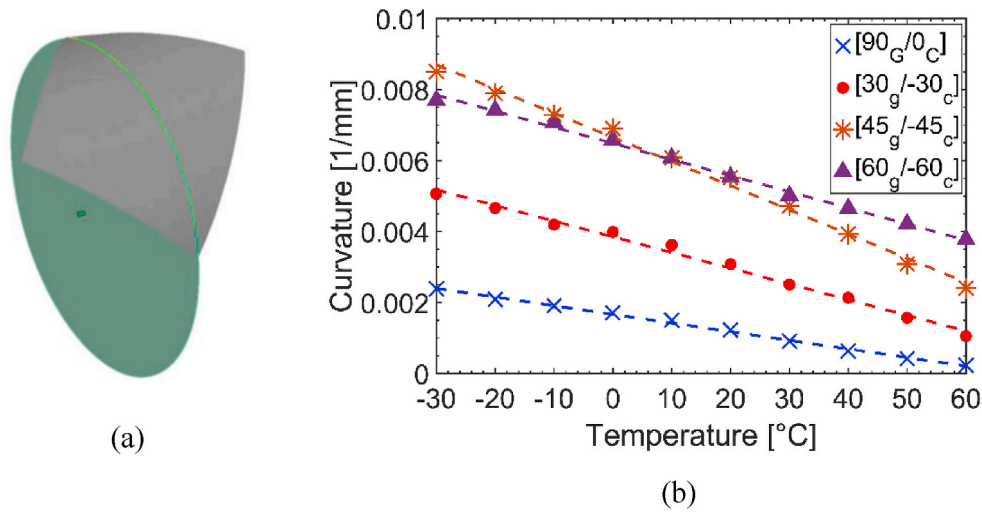


Fig. 8. (a) schematic representation of the osculating circle, and (b) curvature vs temperature for laminates and least square fitted lines.

Table 4
Slopes of fitted lines on the curvature vs temperature data for each laminate.

Laminate	[90 _g /0 _c]	[30 _g /-30 _c]	[45 _g /-45 _c]	[60 _g /-60 _c]
Slopes [1/mm.°C]	-2.4×10^{-5}	-4.42×10^{-5}	-6.81×10^{-5}	-4.54×10^{-5}

where $E_{1\theta}$ and $E_{2\theta}$ are the axial elastic modulus of layer 1 and 2 in θ direction, $\alpha_{1\theta}$ and $\alpha_{2\theta}$ are CTE of layers in θ direction, ΔT is the temperature difference between deformed and initial configurations. Herein, due to the pre-curvature state of the composite structure at ambient temperature, a correction formula is needed to account for flattening of the pre-curved state of composite in response to increase in temperature [42]. Therefore, the radius of curvature of the morphing

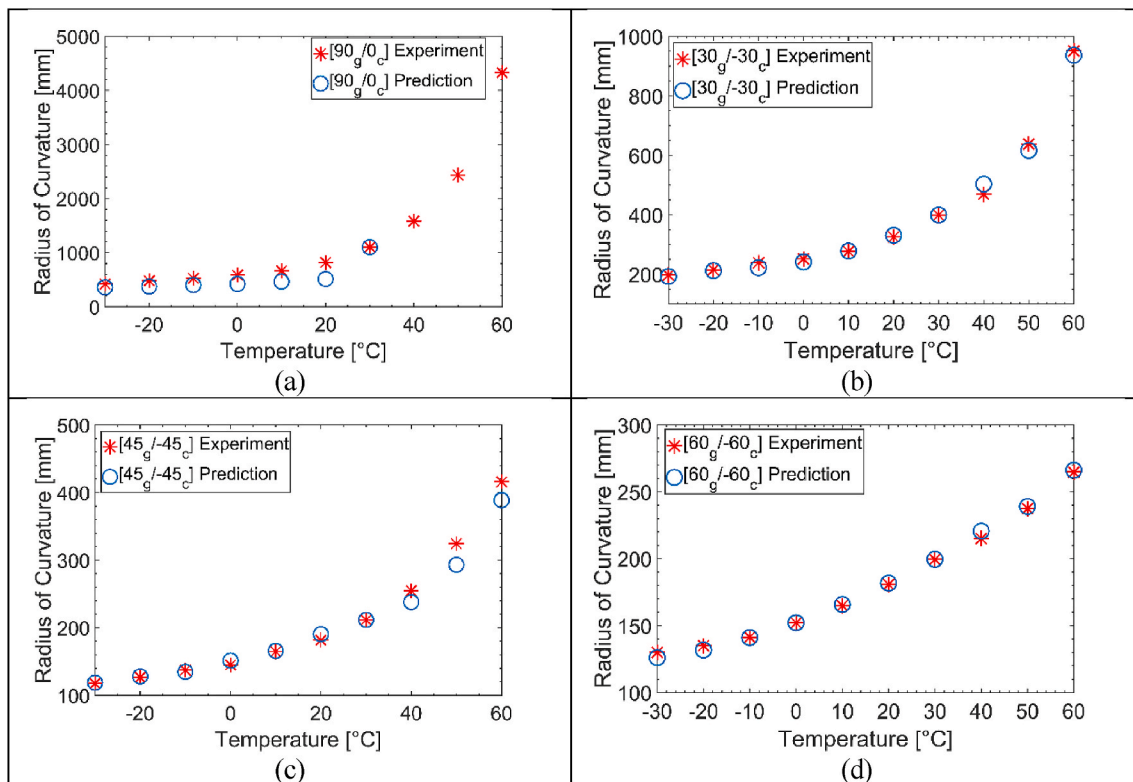


Fig. 9. Radius of curvature vs. temperature; comparison between Theoretical prediction by Timoshenko formula and experimental measurements.

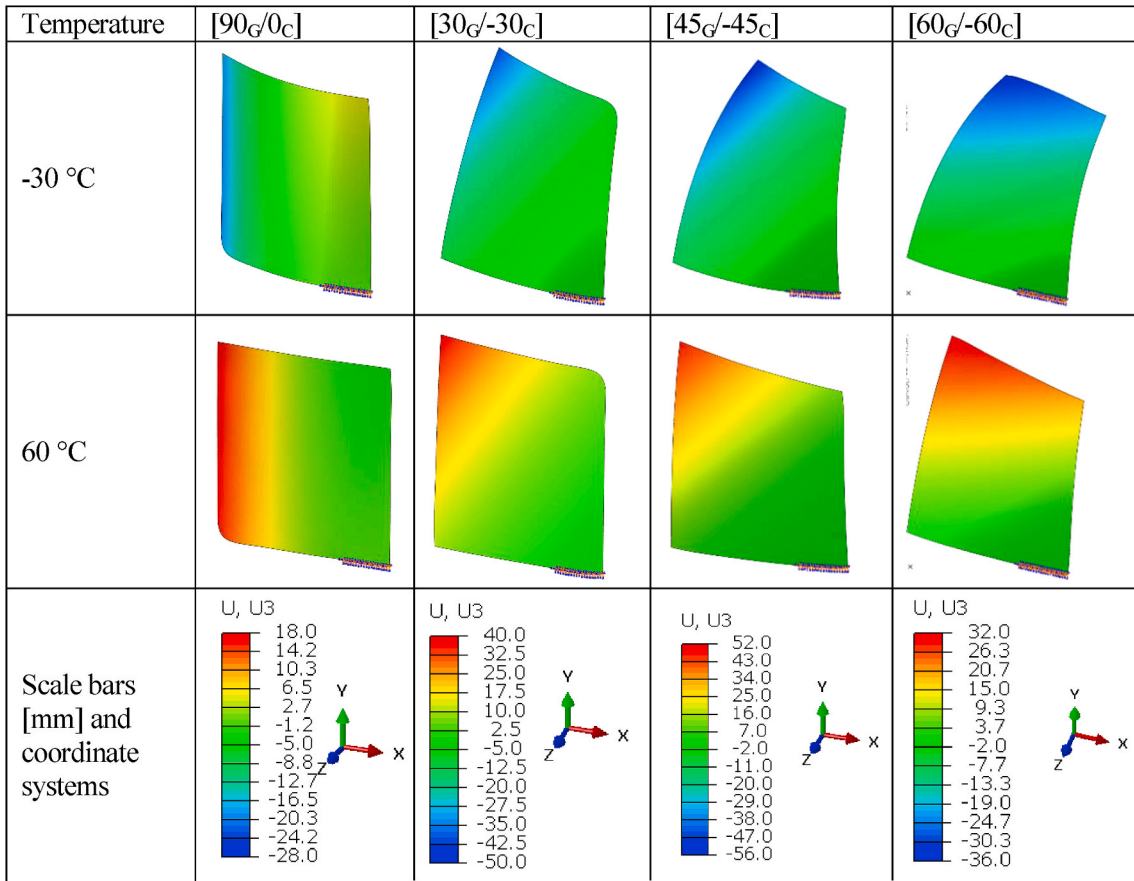


Fig. 10. FEA simulated full-field morphing behaviour of laminates with different fibre directionally between -30 °C and 60 °C.

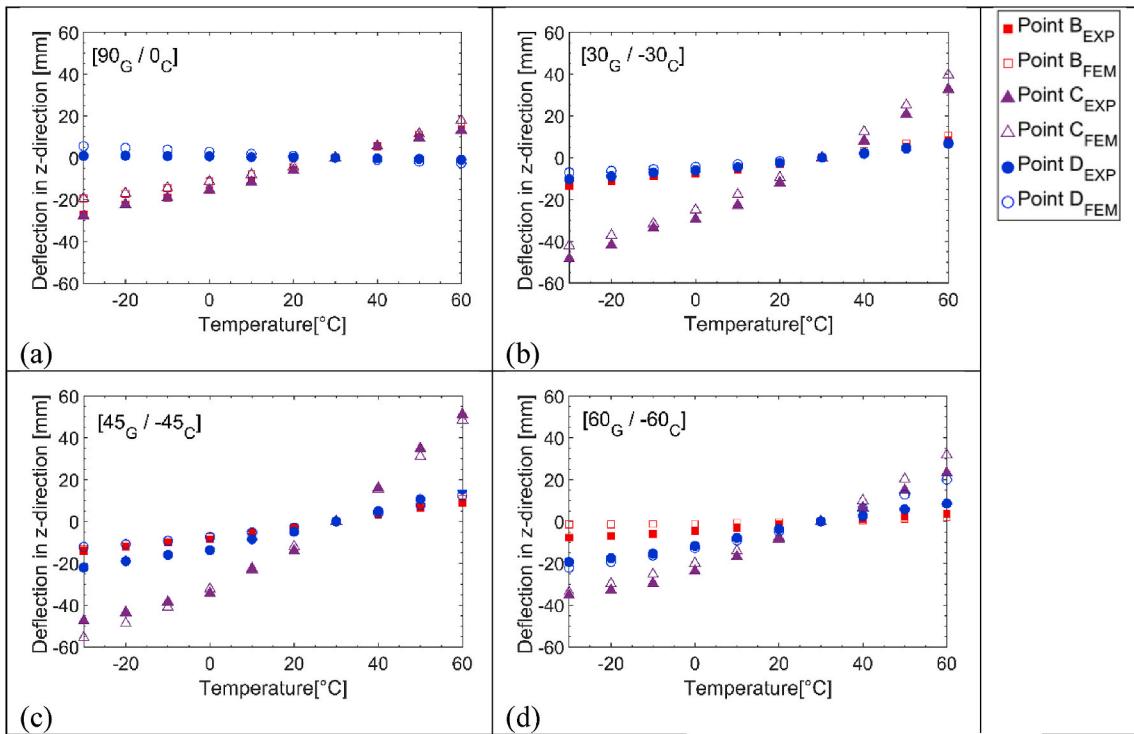


Fig. 11. Simulation prediction and experimentally measured displacement in z direction for three points of B, C, D in each laminate.

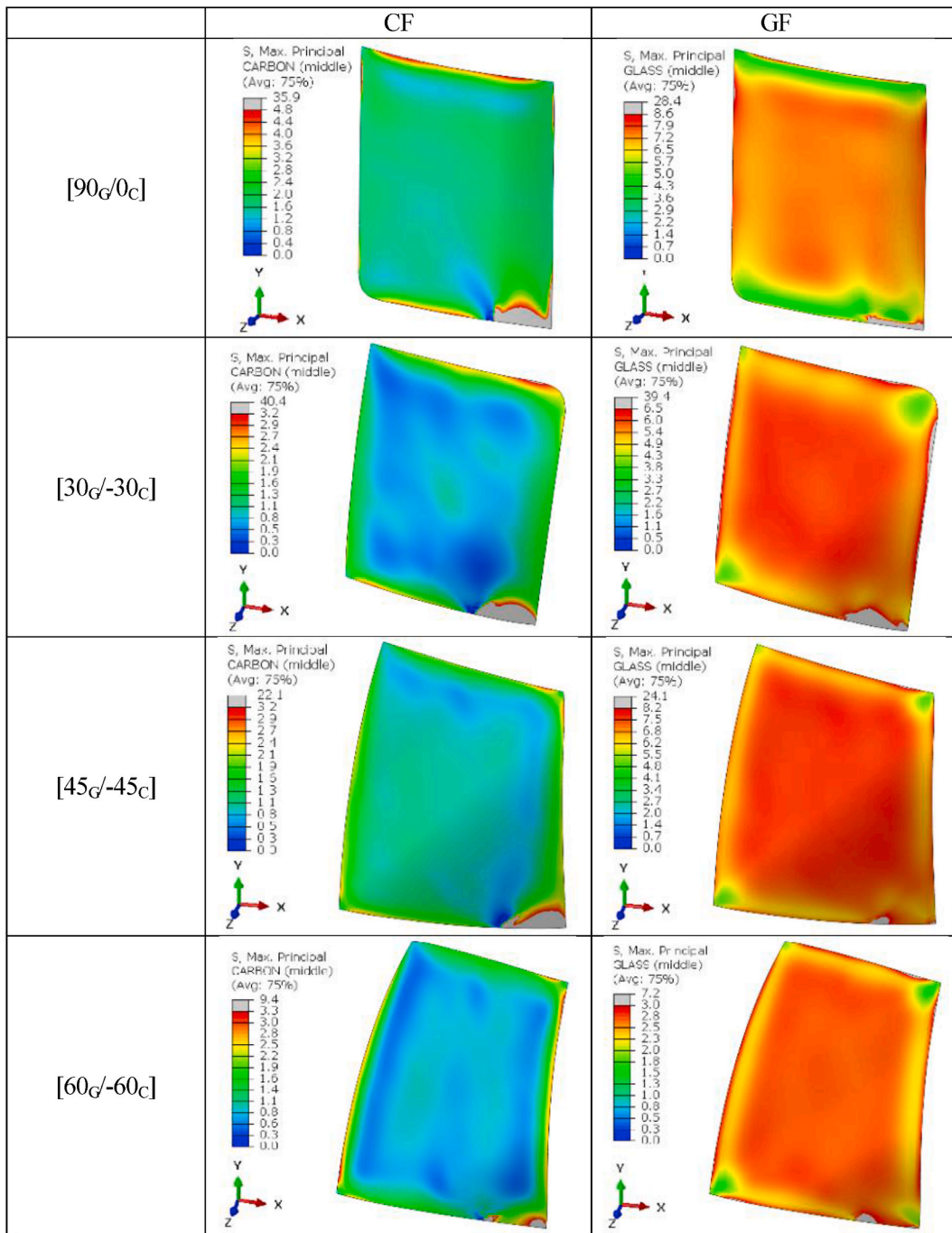


Fig. 12. Maximum principal stress (tensile) distribution calculated by FEA simulations at -30°C .

composite for other temperatures is calculated as [42]:

$$R_h = \frac{kR_c}{k - R_c} \tag{13}$$

where R_h is the radius of curvature after temperature change, R_c is the experimentally determined radius of curvature and k is the radius of curvature obtained from Eq (12). The prediction of the radius of curvature of the composite with Timoshenko formula is presented with hollow circles while experimental values obtained by DIC are shown with red stars in Fig. 9, which conveys the close agreement of predicted values to the experimental observation. It should be noted that k value for $[90_G/0_C]$ laminates at temperature ranges higher than 30°C are higher than R_c which makes the model unable to predict curvature at

this temperature range for this specific laminate.

3.5. Finite element analysis and verification

To further understand the mechanism of morphing behaviour, numerical modelling based on FEA was performed by using ABAQUS™ commercial software on each laminate. FEA is a powerful technique that, together with experiments, can be used to unravel the effective parameters and underlying driving forces for morphing behaviour. The initial curvature of each laminate was attained from DIC at 30°C and used as a feed in FEA. Then laminates behaviour and their displacements were tracked under different temperature conditions. Fig. 10 displays the FEA results of displacement for laminates at -30°C and 60°C while Fig. S2 shows the displacement on other temperatures including 0°C

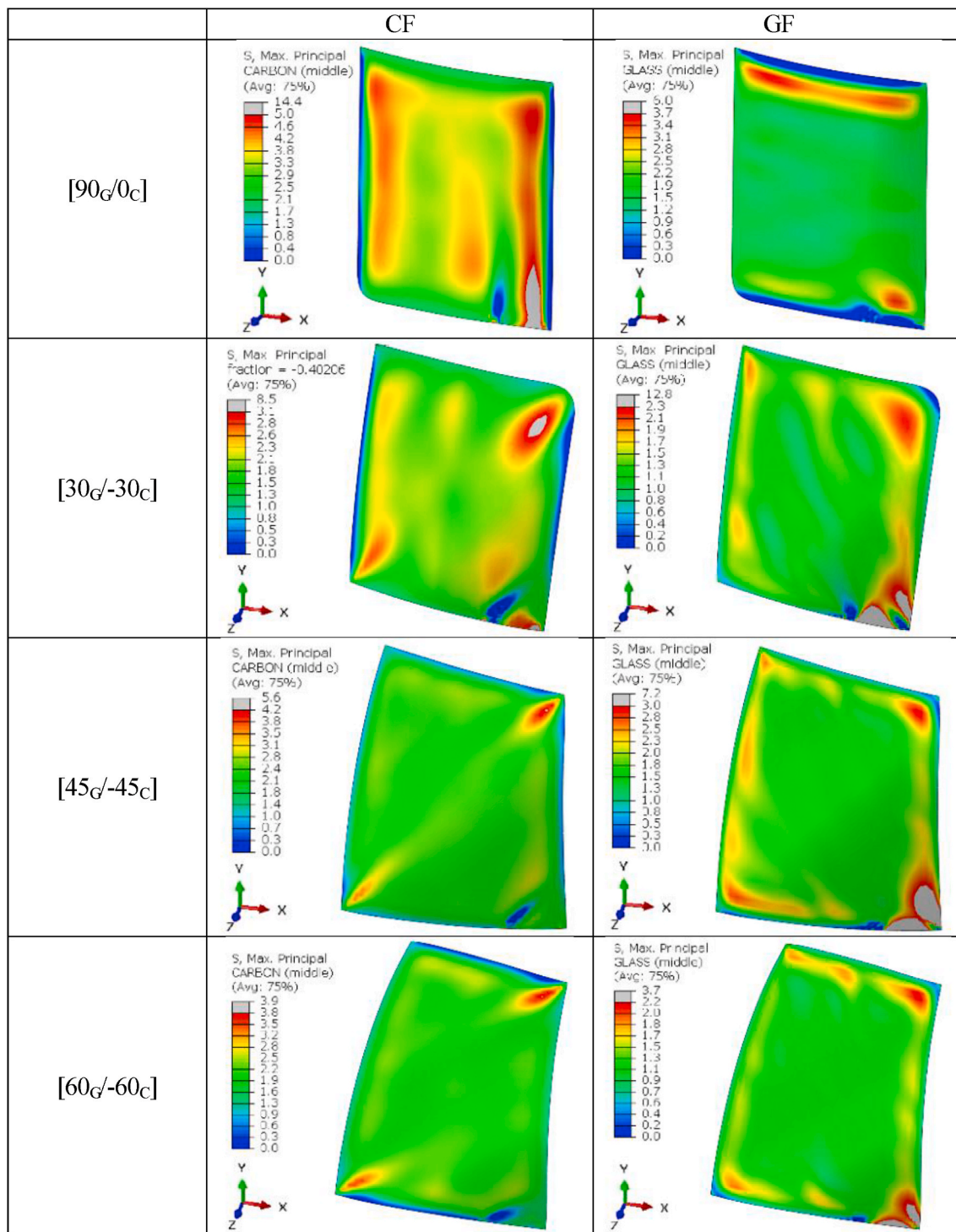


Fig. 13. Maximum principal stress (tensile) distribution calculated by FEA simulations at 60 °C.

and 30 °C. The displacements level and morphing behaviour obtained by FEA simulation presented in Fig. 10 are in close agreement with experimental data demonstrated in Fig. 7. However, to further verify the accuracy and reliability of the analyses, displacement in the z-direction for three points of B, C, D of each laminate were compared with experimental outcomes obtained by DIC for temperatures in the range of -30 °C and 60 °C with 10 °C intervals, as shown in Fig. 11. The negligible deviation of the predicted results from experimental observation confirms the reliability of the model.

3.6. Internal stress distributions and its correlation with morphing

The validated FEA were used to extract information on the stress distribution over the laminates and on the individual laminae and to investigate its effect on morphing behaviour. Maximum and minimum principal stresses on CF and GF layers at each laminate at -30 °C and 60 °C are shown in Figs. 12–15 and more details are available in Figs. S3–S6. The principal stresses were obtained by choosing a basis in which the shear stress components of the stress tensor vanish [43]. It is worth noting that the maximum principal stress represents the most

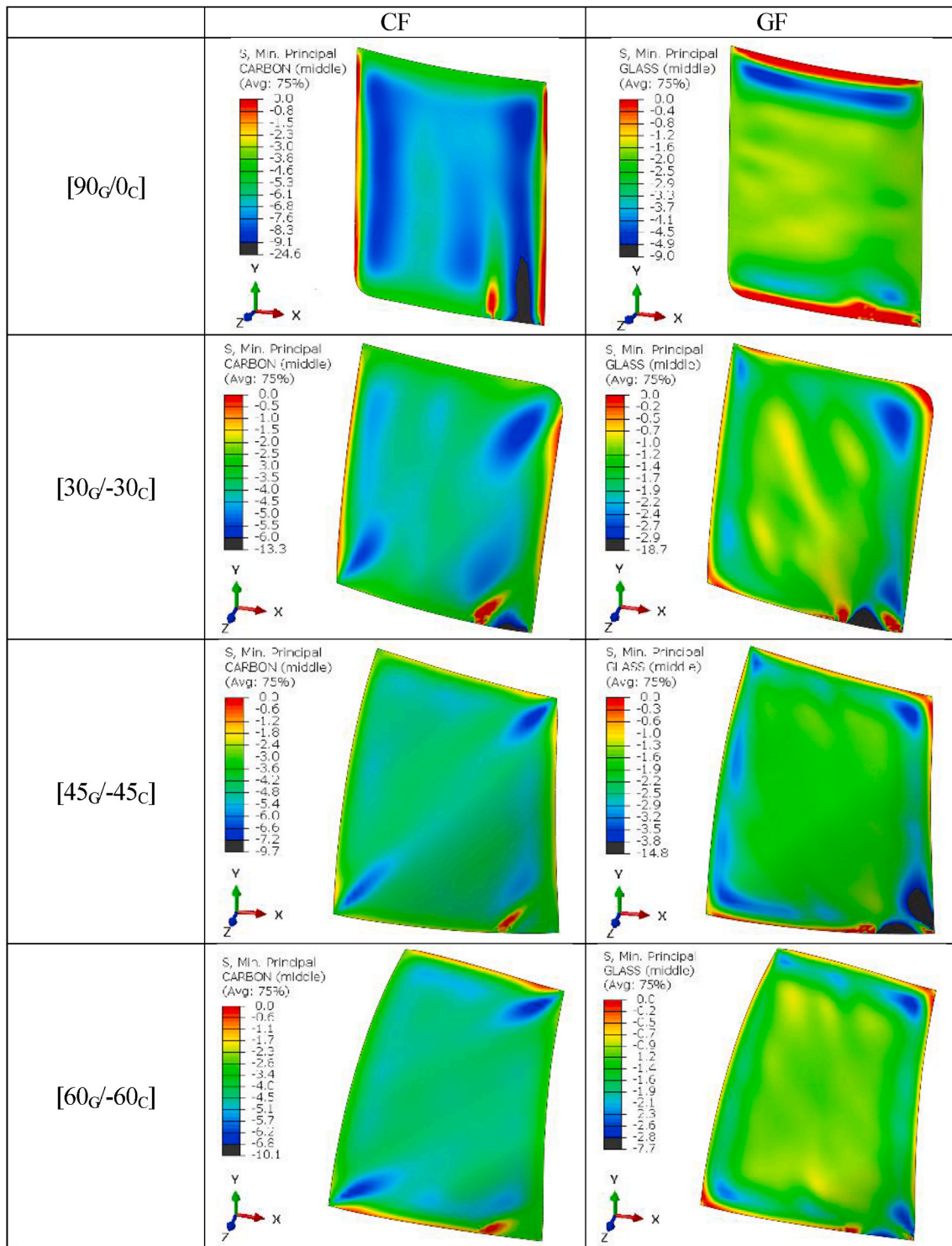


Fig. 14. Minimum principal stress (tensile) distribution calculated by FEA simulations at -30°C .

tensile and the minimum principal stress is an indication most compressive stresses. It is seen that principal stress distributions were not uniform in the laminas and it was highly temperature and fibre orientation dependent. The grey regions in Figs. 12–15 at the bottom right are demonstrating higher principal stress values due to the gripping of the plates from those regions as it is also demonstrated in Fig. 10 with crosses at the same position. In $[90_G/0_C]$ laminate, CF layer at -30°C showed a higher value of maximum principal stress at upper and lower edges (alongside A-B and C-D lines) while it was lower at the areas

close to B-C line, as seen in Figs. 12 and 13. Moreover, the maximum principal stress at the GF layer of the same laminate was relatively higher than the CF layer while similar to the CF layer it showed lower values at upper and lower edges and concentration at middle area. Figs. 14 and 15 reveal that CF layer is under compressive stress while GF layer shows lower values of minimum principal stresses or compression at -30°C . However, increasing the temperature to 60°C resulted in the increase of the radius of curvature reversed the pattern and put the CF under tensile stress and GF under compression which is in agreement

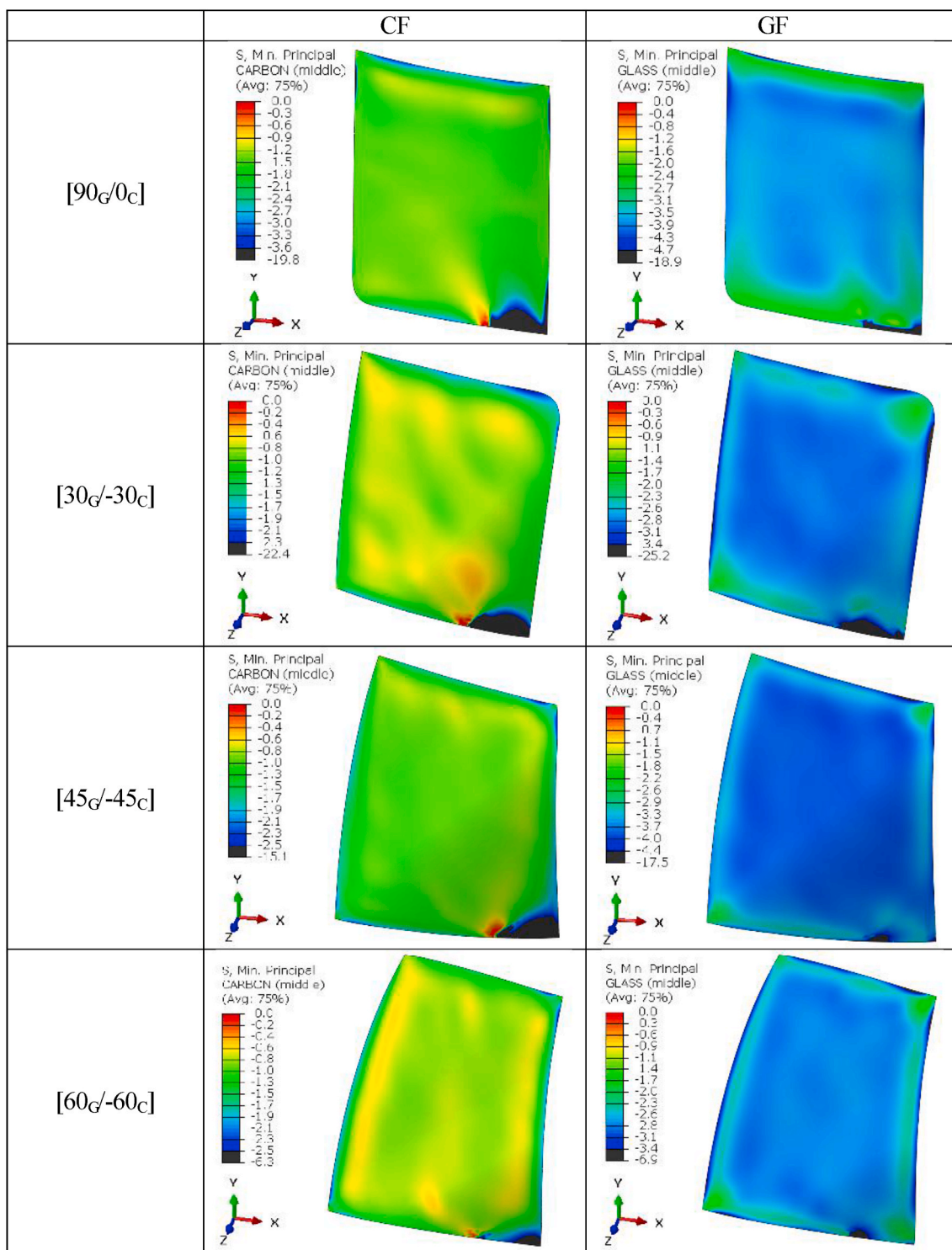


Fig. 15. Minimum principal stress (tensile) distribution calculated by FEA simulations at 60 °C.

with the principles of classical bending beam theory [38]. The overall (global) tensile and compressive stresses trends for all laminates were following a similar pattern as described for [90_G/0_C] laminate. However, it is seen that the direction of fibre influences the local stress distributions. In addition, the maximum principal stresses of both GF and CF at 60 °C and minimum principal stresses at -30 °C of each layer showed a non-uniformity on principal stress and alignment with fibre direction of that layer indicating the dominance of tensile and compression stresses in fibre direction at each lamina, respectively.

4. Conclusions

The shape morphing behaviour of CF/GF/epoxy asymmetric composite laminates with different fibre directionalities of [90_G/0_C], [30_G/-30_C], [45_G/-45_C], and [60_G/-60_C] was studied experimentally, theoretically and numerically. To do so, unidirectional CF and GF prepregs were used to manufacture asymmetric and shape morphing laminates using vacuum bagging method and by curing them at the temperature of 130 °C. Mechanical and physical properties of each type of CF and GF laminates were investigated along and transverse to fibre direction and

classical laminate theory was used to calculate the CTE and elastic modulus for different angles relative to the fibre direction as the essential properties to control the morphing behaviour. DIC full-field displacement monitoring was used to evaluate the morphing behaviour of laminates with different microstructure between temperatures ranging from -30°C to 60°C . The non-contact principle and full-field monitoring capability of DIC minimized the measurement errors due to the variation in the sample temperature and enabled the monitoring for the morphing behaviour of complex geometries. The variation of the curvature at different temperatures and the relations between morphing behaviour and its temperature dependency to the microstructure of each laminate were discussed. Timoshenko bimetallic strip formula was adapted to predict the curvature in pre-curved composite laminates successfully and its limitations are mentioned. FEA was used to predict the morphing behaviour and to study the maximum and minimum principal stresses at each layer for different laminates which provided an insight on structural mechanisms involved in morphing behaviour of fibre reinforced composite structures. The findings of this study are believed to contribute to the state of the art significantly by improving of our understandings on morphing behaviour of fibre-reinforced composite and correlating it with microstructure of laminates.

Author statement

Jamal Seyyed Monfared Zanjani: Conceptualization, Methodology, Formal analysis, Resources, Writing - Original Draft, Writing - Review & Editing, Supervision, Funding acquisition. **Pouya Yousefi Louyeh:** Conceptualization, Methodology, Formal analysis, Data Curation, Validation, Writing - Original Draft. **Isa Emami Tabrizi:** Conceptualization, Methodology, Formal analysis, Data Curation, Validation, Writing - Original Draft. **Abdulrahman Saeed Al-Nadhari:** Data Curation. **Mehmet Yildiz:** Supervision, Funding acquisition, Writing - Review & Editing.

Note

Jamal Seyyed Monfared Zanjani, Pouya Yousefi Louyeh, and Isa Emami Tabrizi contributed equally to this work.

Declaration of competing interest

The authors declare that they have no known competing financial interests or personal relationships that could have appeared to influence the work reported in this paper.

Appendix A. Supplementary data

Supplementary data to this article can be found online at <https://doi.org/10.1016/j.tws.2020.106874>.

References

- [1] G. Marsh, Composites consolidate in commercial aviation, *Reinforc Plast* 60 (5) (2016) 302–305.
- [2] A.J. Timmis, A. Hodzic, L. Koh, M. Bonner, C. Soutis, A.W. Schäfer, L. Dray, Environmental impact assessment of aviation emission reduction through the implementation of composite materials, *Int. J. Life Cycle Assess.* 20 (2) (2015) 233–243.
- [3] J.S. Monfared Zanjani, B.S. Okan, Y.Z. Menceloglu, M. Yildiz, Nano-engineered design and manufacturing of high-performance epoxy matrix composites with carbon fiber/selectively integrated graphene as multi-scale reinforcements, *RSC Adv.* 6 (12) (2016) 9495–9506.
- [4] J.S.M. Zanjani, B. Saner Okan, Y.Z. Menceloglu, M. Yildiz, Design and fabrication of multi-walled hollow nanofibers by triaxial electrospinning as reinforcing agents in nanocomposites, *J. Reinforc. Plast. Compos.* 34 (16) (2015) 1273–1286.
- [5] N. Forintos, T. Czigany, Multifunctional application of carbon fiber reinforced polymer composites: electrical properties of the reinforcing carbon fibers – a short review, *Compos. Part B Eng.* 162 (2019) 331–343.
- [6] S. Ganguli, A.K. Roy, D.P. Anderson, Improved thermal conductivity for chemically functionalized exfoliated graphite/epoxy composites, *Carbon* 46 (5) (2008) 806–817.
- [7] M. Ullah, J. Seyyed Monfared Zanjani, L. Haghighi Poudeh, M. Siddiq, B. Saner Okan, M. Yildiz, Y. Menceloglu, Manufacturing functionalized mono-crystalline diamond containing electrospun fibers reinforced epoxy composites with improved mechanical characteristics, *Diam. Relat. Mater.* 76 (2017) 90–96.
- [8] J. Seyyed Monfared Zanjani, B. Saner Okan, P.-N. Pappas, C. Galiotis, Y. Z. Menceloglu, M. Yildiz, Tailoring viscoelastic response, self-heating and deicing properties of carbon-fiber reinforced epoxy composites by graphene modification, *Compos. Part A Appl. Sci. Manuf.* 106 (2018) 1–10.
- [9] J.S. Monfared Zanjani, B.S. Okan, I. Letofsky-Papst, Y. Menceloglu, M. Yildiz, Repeated self-healing of nano and micro scale cracks in epoxy based composites by tri-axial electrospun fibers including different healing agents, *RSC Adv.* 5 (89) (2015) 73133–73145.
- [10] J. Seyyed Monfared Zanjani, B. Saner Okan, C. Yilmaz, Y. Menceloglu, M. Yildiz, Monitoring the interface and bulk self-healing capability of tri-axial electrospun fibers in glass fiber reinforced epoxy composites, *Compos. Part A Appl. Sci. Manuf.* 99 (2017) 221–232.
- [11] J. Seyyed Monfared Zanjani, A.S. Al-Nadhari, M. Yildiz, Manufacturing of electroactive morphing carbon fiber/glass fiber/epoxy composite: process and structural monitoring by FBG sensors, *Thin-Walled Struct.* 130 (2018) 458–466.
- [12] V.Q. Nguyen, A.S. Ahmed, R.V. Ramanujan, Morphing soft magnetic composites, *Adv. Mater.* 24 (30) (2012) 4041–4054.
- [13] E. Munch, M.E. Launey, D.H. Alsem, E. Saiz, A.P. Tomsia, R.O. Ritchie, Tough, bio-inspired hybrid materials, *Science* 322 (5907) (2008) 1516–1520.
- [14] W. Raither, M. Heymanns, A. Bergamini, P. Ermanni, Morphing wing structure with controllable twist based on adaptive bending-twist coupling, *Smart Mater. Struct.* 22 (6) (2013), 065017.
- [15] A.R. Studart, R.M. Erb, Bioinspired materials that self-shape through programmed microstructures, *Soft Matter* 10 (9) (2014) 1284–1294.
- [16] R. Elbaum, L. Zaltzman, I. Burgert, P. Fratzl, The role of wheat awns in the seed dispersal unit, *Science* 316 (5826) (2007) 884–886.
- [17] P. Fratzl, R. Elbaum, I. Burgert, Cellulose fibrils direct plant organ movements, *Faraday Discuss* 139 (2008) 275–282 (0).
- [18] W. Hufenbach, M. Gude, Analysis and optimisation of multistable composites under residual stresses, *Compos. Struct.* 55 (3) (2002) 319–327.
- [19] S. Daynes, P.M. Weaver, Design and testing of a deformable wind turbine blade control surface, *Smart Mater. Struct.* 21 (10) (2012) 105019.
- [20] D. Li, S. Zhao, A. Da Ronch, J. Xiang, J. Drofelnik, Y. Li, L. Zhang, Y. Wu, M. Kintscher, H.P. Monner, A. Rudenko, S. Guo, W. Yin, J. Kirn, S. Storm, R. D. Breuker, A review of modelling and analysis of morphing wings, *Prog. Aero. Sci.* 100 (2018) 46–62.
- [21] L. Ren, A. Parvizi-Majidi, Z. Li, Cured shape of cross-ply composite thin shells, *J. Compos. Mater.* 37 (20) (2003) 1801–1820.
- [22] M.-L. Dano, M.W. Hyer, Thermally-induced deformation behavior of unsymmetric laminates, *Int. J. Solid Struct.* 35 (17) (1998) 2101–2120.
- [23] M. Schlecht, K. Schulte, Advanced calculation of the room-temperature shapes of unsymmetric laminates, *J. Compos. Mater.* 33 (16) (1999) 1472–1490.
- [24] A.J. Lee, A. Moosavian, D.J. Inman, A piezoelectrically generated bistable laminate for morphing, *Mater. Lett.* 190 (2017) 123–126.
- [25] S. Daynes, C.G. Diaconu, K.D. Potter, P.M. Weaver, Bistable prestressed symmetric laminates, *J. Compos. Mater.* 44 (9) (2010) 1119–1137.
- [26] Z. Zhang, H. Wu, G. Ye, J. Yang, S. Kitipornchai, G. Hai, Experimental study on bistable behaviour of anti-symmetric laminated cylindrical shells in thermal environments, *Compos. Struct.* 144 (2016) 24–32.
- [27] I.E. Tabrizi, A. Kefal, J.S.M. Zanjani, C. Akalin, M. Yildiz, Experimental and numerical investigation on fracture behavior of glass/carbon fiber hybrid composites using acoustic emission method and refined zigzag theory, *Compos. Struct.* 223 (2019), 110971.
- [28] V.S.C. Chillara, M.J. Dapino, Stability considerations and actuation requirements in bistable laminated composites, *Compos. Struct.* 184 (2018) 1062–1070.
- [29] S. Barbarino, F. Gandhi, S.D. Webster, Design of extendable chord sections for morphing helicopter rotor blades, *J. Intell. Mater. Syst. Struct.* 22 (9) (2011) 891–905.
- [30] J. Riemenschneider, C. Balzarek, B.G. van der Wall, R.K. Majeti, Chord Morphing for Helicopter Rotor Blades, 2019.
- [31] L.Y. Matloff, E. Chang, T.J. Feo, L. Jeffries, A.K. Stowers, C. Thomson, D. Lentink, How flight feathers stick together to form a continuous morphing wing, *Science* 367 (6475) (2020) 293.
- [32] V.S.C. Chillara, L.M. Headings, R. Tsuruta, E. Itakura, U. Gandhi, M.J. Dapino, Shape memory alloy-actuated prestressed composites with application to morphing automotive fender skirts, *J. Intell. Mater. Syst. Struct.* 30 (3) (2018) 479–494.
- [33] Y. Gandhi, A. Pironi, L. Collini, Analysis of bistable composite laminate with embedded SMA actuators, *Procedia Struct. Integr.* 12 (2018) 429–437.
- [34] R. Marques, M. Unel, M. Yildiz, A. Suleman, Remaining useful life prediction of laminated composite materials using Thermoelastic Stress Analysis, *Compos. Struct.* 210 (2019) 381–390.
- [35] Acquisition Basic-GOM Software 2016 Manual Germany (GOM mbH B).
- [36] M.W. Hyer, S.R. White, Stress Analysis of Fiber-Reinforced Composite Materials, DEStech Publications, Inc, 2009.
- [37] H.W. Wang, H.W. Zhou, L.L. Gui, H.W. Ji, X.C. Zhang, Analysis of effect of fiber orientation on Young's modulus for unidirectional fiber reinforced composites, *Compos. Part B Eng.* 56 (2014) 733–739.

- [38] K. Chung, M.-G. Lee, Pure bending and beam theory, in: K. Chung, M.-G. Lee (Eds.), *Basics of Continuum Plasticity*, Springer Singapore, Singapore, 2018, pp. 73–109.
- [39] R. De Oliveira, S. Lavanchy, R. Chatton, D. Costantini, V. Michaud, R. Salathé, J.-A. Manson, Experimental investigation of the effect of the mould thermal expansion on the development of internal stresses during carbon fibre composite processing, *Compos. Part A Appl. Sci. Manuf.* 39 (7) (2008) 1083–1090.
- [40] S. Timoshenko, Analysis of Bi-metal thermostats, *J. Opt. Soc. Am.* 11 (3) (1925) 233–255.
- [41] G.D. Angel, G. Haritos, I.S. Campbell, Spatial prediction of a pre-curved bimetallic strip under combined loading, in: G.-C. Yang, S.-I. Ao, L. Gelman (Eds.), *Transactions on Engineering Technologies*, Springer Netherlands, Dordrecht, 2014, pp. 227–240.
- [42] G. Angel, G. Haritos, I. Campbell, Straightening locus of a curved bimetallic strip subjected to heating, in: *Proceedings of the World Congress on Engineering*, 2013.
- [43] A. Evans, M. Prestat, R. Tölke, M.V.F. Schlupp, L.J. Gauckler, Y. Safa, T. Hocker, J. Courbat, D. Briand, N.F.d. Rooij, D. Courty, Residual stress and buckling patterns of free-standing Yttria-stabilized-zirconia membranes fabricated by pulsed laser deposition, *Fuel Cell.* 12 (4) (2012) 614–623.